



## Generalized moving boundary model for charge–discharge of LiFePO<sub>4</sub>/C cells



Ashish Khandelwal<sup>a</sup>, Krishnan S. Hariharan<sup>a,\*</sup>, V. Senthil Kumar<sup>a</sup>, Priya Gambhire<sup>a</sup>, Subramanya Mayya Kolake<sup>a</sup>, Dukjin Oh<sup>b</sup>, Seokgwang Doo<sup>b</sup>

<sup>a</sup> Computational Simulations Group, SAIT-India Lab, TRIDIB – Bagmane Tech Park, Bangalore 560 093, India

<sup>b</sup> Energy Storage Group, Samsung Advanced Institute of Technology, 449712, South Korea

### HIGHLIGHTS

- Generalized moving boundary model for lithium ion cells with phase change electrode.
- Numerical implementation is obtained using a pseudo 2D approach.
- Model captures tangential phase front movement and phase separation in LiFePO<sub>4</sub>.
- Simulation shows charge–discharge asymmetry and path dependency in LiFePO<sub>4</sub>.

### ARTICLE INFO

#### Article history:

Received 28 June 2013

Received in revised form

10 September 2013

Accepted 16 September 2013

Available online 26 September 2013

#### Keywords:

Lithium ion battery

Phase transition models

Moving boundary problem

Lithium iron phosphate

Electrochemical model

### ABSTRACT

Lithium ion cells with electrode materials that undergo phase transitions, like LiFePO<sub>4</sub>, have unique charge–discharge characteristics. In this work a generalized framework of moving boundary approach is proposed to model the path dependent charge–discharge response of porous electrodes that exhibit multi-phase coexistence. Using the Landau transformation the governing equation in moving coordinate is transformed to fixed coordinate and a suitable path dependent algorithm is devised and is implemented in a multi-physics environment. Simulation results show that tangential propagation of the phase front, often seen in experiments, can be addressed by this model. Incorporation of multi-phase diffusion predicts the characteristic phase separation in LiFePO<sub>4</sub> particles. The proposed model successfully captures the charge–discharge asymmetry of LiFePO<sub>4</sub> based cells. Efficacy of the proposed approach to model the path dependence of cells with phase change electrodes is demonstrated by simulating the response of LiFePO<sub>4</sub>/graphite cell subjected to a charge–discharge pulse. Numerical studies are performed to study the effect of important model parameters to enhance cell design and to bring out unique features in the cell response due to multi-phase coexistence.

© 2013 Elsevier B.V. All rights reserved.

## 1. Introduction

Lithium iron phosphate (LiFePO<sub>4</sub>, LFP) is increasingly deployed as positive electrode material in lithium ion cells owing to its high thermal stability, cost effectiveness, non-toxic nature and long cycle life [1–3]. Given these advantages, it however suffers from limitations [4–6] due to low electronic conductivity resulting in higher Ohmic drop in the electrode and low rate capability leading to reduced active material utilization. Several research efforts over the last decade have enabled significant improvements by

enhancing properties of the material through suitable modifications. Some of the prominent ideas pertain to coating of LFP particles with carbon to improve electronic conductivity [7,8], decrease in particle size for reduction in transport losses [9,10], use of LFP nano-crystals to increase the surface area [11], solid–solution doping by polyvalent metals [12] etc. Because of these developments, LFP based cells have found applications in mobile, automotive and other industries.

The wide spectrum of applications of LFP based cells encourages electrochemical modeling to understand the underlying cell processes. In addition to optimized cell design, electrochemical models enable robust battery management systems (BMS) development for on-board applications. A critical challenge in developing BMS algorithm for cells with LFP based electrodes is the non-monotonic dependence of open circuit potential on capacity. This behavior is

\* Corresponding author.

E-mail addresses: [krishnan.sh@samsung.com](mailto:krishnan.sh@samsung.com), [krishnan.sh@gmail.com](mailto:krishnan.sh@gmail.com) (K.S. Hariharan).

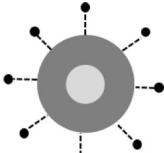
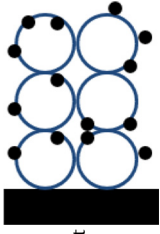
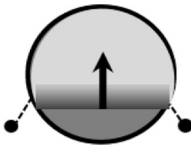
also observed in other electrode materials, mainly due to the underlying crystallographic solid–solid phase transformation. Therefore, modeling phase change is an active area of research that enables development of a complete electrochemical model [8] for lithium based cells. These models are proposed at various length scales varying from crystalline level to continuum level. Existing approaches in electrochemical modeling of LFP electrodes can be classified into three categories viz., (a) shrinking core models [13–18], (b) phase field models [19–23], and (c) resistive reactant models [24–28]. A brief overview of these models is provided in Table 1.

An electrochemical model based on a core–shell approach was first proposed for LFP electrode by Srinivasan and Newman [14] and later developed [15] for an LFP/C cell. As mentioned in Table 1, this approach captures the discharge behavior by considering intercalation coupled mass transport due to diffusion in a Li rich  $\beta$  phase and movement of two-phase interface. In this framework however, the diffusion in Li-poor phase ( $\alpha$ ) is neglected. The underlying construct of this model assumes diffusion in a particle causing lithium flux movement normal to the phase boundary. On the contrary, experimental studies [1] reveal Li movement in a tangential direction. The diffusion under phase transition is modeled using sharp interface model which predicts a fast Li transfer across the phase boundary between  $\alpha$  and  $\beta$  phase. Followed by this work, a more sophisticated version of the core–shell model in which diffusion in both phases of  $\text{LiCoO}_2$  cathode [13] is developed. Also, Wang and co-workers in Ref. [16], proposed a model for LFP, where the interface movement between the two coexisting phases was considered to be sluggish by incorporating a mobility term in the interface movement equation. Kasavajjula [17] further enhanced this model by considering the Li diffusion in both phases together along with the interface mobility. Recently, a multi-scale approach proposed by Dargaville and Farrell [18] employed the shrinking-core model of Srinivasan and Newman [14] to represent the three size scales present in a porous LFP cathode, namely crystals, agglomerates, and the porous cathode itself.

Above developments show that the core–shell approach provides a mathematically consistent framework to incorporate effects of phase transitions in a complete electrochemical model. The existing models [13–18] do not however account for factors such as diffusion in the Li-poor LFP phase ( $\alpha$ ), Ohmic drop due to carbon coating to model inhomogeneous current distribution etc. As a result, the application of the shrinking core approach is limited to represent discharge behavior only. Safari and Delacourt [26,27] recently proposed a reduced order electrochemical model using the resistive reactant concept without incorporating the details of phase transformation in LFP electrode. It successfully captures the charge–discharge asymmetry but does not represent the features due to phase transformation in terms of tangential front propagation, phase separation and path dependence. Hence, development of a suitable electrochemical approach that models the multi-phase coexistence during charge and discharge consistently is highly desirable. Considering the simple and robust framework of shrinking core model an extension of this approach to represent multiple charge–discharge cycle is yet to be attempted. Such a general framework would also enable detailed investigation of charge–discharge asymmetry and path dependence [29] frequently reported for LFP electrodes.

In the present work a general electrochemical framework is proposed that identifies the mechanisms governing voltage response in cells with phase change electrodes. In the following sections, a generalized path dependent moving boundary model is developed and subsequently modified as a cell design tool. Section 2 describes the phase transformation processes in LFP which brings

**Table 1**  
An overview of existing electrochemical models for LFP.

Technique	
	
	
Principle	Non-local chemical potential is used to ascribe diffusion
Seminal Work	Singh, Ceder and Bazant [19]
Pros	1. Models observed tangential phase front propagation 2. Diffused interface description 1. Computationally elaborate 2. Not suited for multiple cycles 3. Needs further development for integration with EM
Cons	Concept of shrinking core is used to model phase transition Padhi, Nanjundaswamy, and Goodenough [1], Srinivasan and Newman [14] 1. Provides physical insight of phase transition 2. Models discharge curves 3. Sharp interface model 1. Normal phase front propagation 2. Inconsistent charge–discharge asymmetry [29] 3. Not suited for multiple cycles
	Non-uniform current distribution due to resistive reactant Ohmic drop Thomas Aleya [24] 1. Models characteristic charge–discharge asymmetry 2. Well suited for multiple cycle application 1. Phase transition is not considered 2. More number of parameters

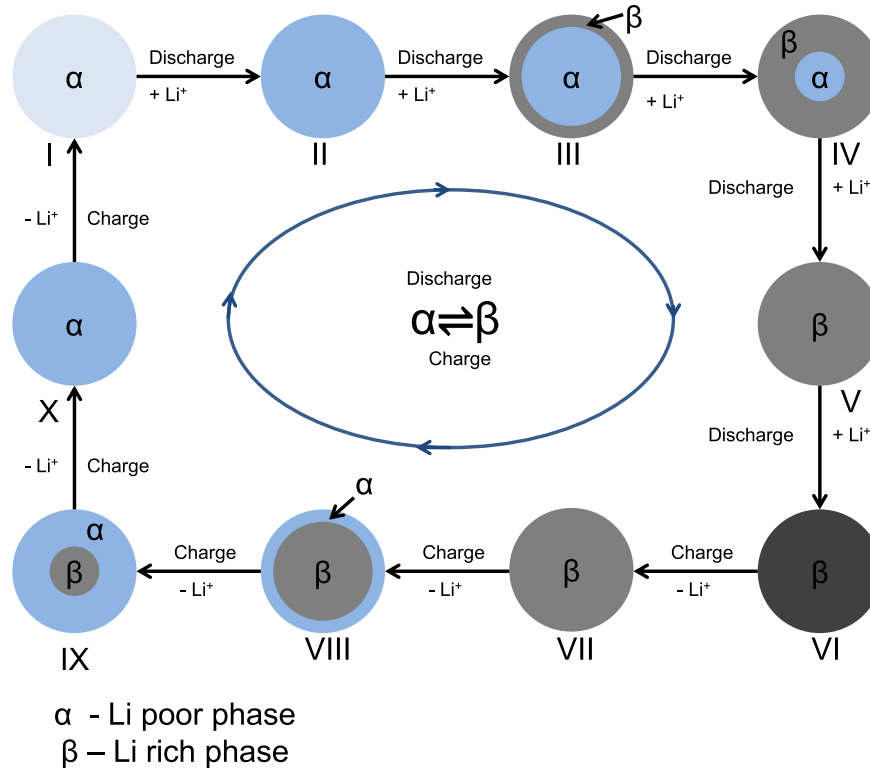


**Fig. 1.** Schematic diagram describing the various stages of lithium intercalation and de-intercalation in LFP during charging and discharging processes based on core-shell construct.

out the physics of path dependence under charge–discharge cycles. Details of the governing equations of the proposed framework are provided in Section 3. In Section 4 the path dependent algorithm is devised and steps involved in numerical implementation are briefly discussed. Section 5 discusses the results obtained from the numerical simulations of proposed model. This section starts with the proposed approach being validated with results [15] reported in literature. Subsequently the charge–discharge asymmetry and path dependency in LFP/C cells are investigated using several case studies. Key insights from the simulations that can be of relevance for optimal cell design are also proposed.

## 2. Phase transformation processes in LFP particle

LFP is naturally available as a phosphate mineral and is an olivine-type material. It has triphylite structure belonging to orthorhombic system of Bravais lattices. Ability to intercalate and de-intercalate lithium ion at desirable range of voltage and current enables application of this material as positive electrode material of secondary lithium ion cells. Interestingly  $LiFePO_4$  is also known to undergo crystallographic structural phase transformation from lithiated triphylite structure (denoted by  $\beta$ ) to de-lithiated heterosite (denoted by  $\alpha$ ) structure during reversible extraction of lithium. Padhi and co-workers [1] discuss the details of the two-phase coexistence and crystallographic structure. Further Dodd [30] and Ramanna [31] use advanced material characterization techniques to provide useful insights. As discussed by Padhi [1], the open circuit voltage curve of  $Li_xFePO_4$  is constant over a large range of values of the intercalate concentration  $x$ . It can be ascertained using the Gibb's phase rule that two phase coexistence drives the underlying intercalation/de-intercalation process resulting in a non-monotonic open circuit voltage. An outcome of the multi-phase coexistence in this material is a path dependent response.

One of the approaches to represent this multi-phase coexistence is a sharp interface (or the core–shell) model.

A schematic of the phase transformation process in LFP is shown in Fig. 1 [29]. Various stages (I–X) during lithiation/delithiation in a two-phase material of spherical geometry is illustrated in Fig. 1 using the core–shell approach. During discharge process, as current is drawn from the cell, lithium intercalates into the de-lithiated LFP particles that constitute the cathode, as shown in stage I and stage II. Onset of phase transformation from de-lithiated  $\alpha$  to lithiated  $\beta$  begins after reaching a critical level of concentration ( $c_{eq}^{\alpha}$ ). This leads to phase separation with a shell of lithium rich  $\beta$  phase forming over the core of lithium poor  $\alpha$  phase, as shown in stage II  $\rightarrow$  III  $\rightarrow$  IV. Stage III and stage IV of schematic Fig. 1 show that during the course of phase transformation the phase separation occurs and core shrinks due to gradual movement of the two phase interface. In phase change materials the mass transfer is directly related to movement of interface which is in turn is related to constant discharge voltage. Phase transformation ceases as the interface reaches the center (Stage V in Fig. 1) phase transformation stops and the material behaves as single phase system. Diffusion in pure  $\beta$  phase continues from stage V to stage VI and the charge transfer reaction stops on successive completion of filling of all de-lithiated sites, and this

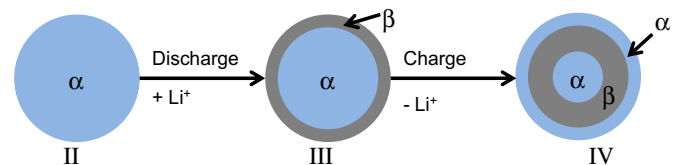


**Fig. 2.** Schematic showing formation of multiple cores and shells in the event of charging of incompletely discharged particle.

marks end of discharge. When the completely discharged or lithiated particle is charged (stage VI), the above described process repeats (stage VI to stage X). The difference during charging is that  $\alpha$  phase forms the shell and  $\beta$  phase forms the core. In contrast to discharging, the single ( $\beta$ ) phase exists for a larger SOC range. During the SOC's when both the phases coexist, the charge transfer reaction occurs in lithium deficient  $\alpha$  phase. From this discussion, it is clear that the diffusion and charge transfer process predominantly occur in different materials during charging and discharging [29] and hence the response different between the processes. This qualitatively explains the existence of asymmetric behavior in LFP particle which is in general a feature [29,32] of any phase changing electrode. More importantly the phase transforming material also shows path dependent response due to multiple phase coexistence. This is further explained using a construct wherein the lithiation process during discharge is not complete and the charging starts. Under such situation shell of lithium poor phase forms (Fig. 2) which can lead to multiple core shell formation and eventually path dependent response. Multiple core shell formation will also accentuate the phase separation and phase inhomogeneity. Quantitative explanation of this behavior is attempted in the present work by devising and numerically solving a generalized moving boundary model in the pseudo 2-D framework of porous electrode theory. Details of the generalized governing equations are given in the next section.

### 3. Electrochemical model for charge–discharge with phase change electrode

Continuum description of coupled electrochemical mass and charge transport in lithium ion cells is obtained using porous electrode theory. Newman [33,34] pioneered this approach and it has led to development of an efficient mathematical tool that captures lithium diffusion dynamics and charge transfer kinetics to predict current/voltage response of a battery. This approach is used to provide design guidelines using theoretical underpinning of thermodynamics, kinetics, and transport across electrodes.

In the Refs. [33–37] details of the model based on porous electrode theory can be found. At the outset, the important assumptions made in porous electrode theory are listed below:

1. Electrode is represented as a superposition of active material, filler, and electrolyte that coexist at every point.
2. Particles of the active material are modeled as spheres.
3. The electrode phase is coupled to the electrolyte phase by the charge transfer reaction.
4. All phases are considered to be electrically neutral.

Based on these assumptions the electrochemical model for lithium ion cell is mathematically described by the following governing partial differential equations (PDEs). These consist of mass transport equation (Eq. (1)), modified Ohm's law for electrolyte (Eq. (2)), Ohm's law for the electrode (Eq. (3)) and Butler–Volmer equation (Eqs. (4) and (5)) which describes reaction-diffusion kinetics that couple the concentration and potential fields of electrode and the electrolyte.

$$\frac{\partial \varepsilon_e c_e}{\partial t} - \nabla \cdot (D_e^{\text{eff}} \nabla c_e) - \frac{1-t_+^0}{F} a_s i_n = 0 \quad (1)$$

$$\nabla \cdot \left( \left( \kappa_e^{\text{eff}} \nabla \phi_e \right) - \frac{2R_g T \kappa_e^{\text{eff}}}{F} (1-t_+^0) \left( 1 + \frac{d \ln f_{\pm}}{d \ln c_e} \right) \nabla \ln c_e \right) + a_s i_n = 0 \quad (2)$$

$$\nabla \cdot (\sigma_s \nabla \phi_s) - a_s i_n = 0 \quad (3)$$

$$i_n = i_0 \left( \exp \left( \frac{\alpha_a F}{R_g T} (\phi_s - \phi_e - U_{eq}) \right) - \exp \left( - \frac{\alpha_c F}{R_g T} (\phi_s - \phi_e - U_{eq}) \right) \right) \quad (4)$$

$$i_0 = F(k_c)^{\alpha_c} (k_a)^{\alpha_a} \left( \frac{c_e}{c_e^{\text{ref}}} \right)^{\alpha_a} (c_{\text{max}} - c_s)^{\alpha_a} c_s^{\alpha_c} \quad (5)$$

It may be noted that the electrodes are treated as homogenized continuum with effective properties given by Bruggeman's relationship. The model equations are adopted for three different zones in the cell viz., anode, separator and cathode based on which the boundary conditions are prescribed. The quantity  $c_s$  appearing in Eq. (5) is the lithium concentration at the surface of the particle, obtained by solving solid phase mass transport equation given by Fick's law. The mass transport equation needs to be modified for materials undergoing phase transformation, as in the present case of LFP particles. Using the sharp interface model the interface coupled diffusion equation [38] in spherical coordinates for materials undergoing phase transition can be expressed as:

$$\frac{\partial c}{\partial t} = \frac{1}{r^2} \frac{\partial}{\partial r} \left( D_i r^2 \frac{\partial c}{\partial r} \right) + \frac{(c_{eq}^p - c_{eq}^s)}{R} v^{s \rightarrow p} \delta(r - r_i^{s \rightarrow p}(t)) \quad (6)$$

$$-D_i \frac{\partial c}{\partial r} \Big|_{r=0} = 0 \quad \forall t \quad (7)$$

$$-D_i \frac{\partial c}{\partial r} \Big|_{r=R} = \frac{i_n}{F} \quad \forall t \quad (8)$$

$$c = c_0|_{t=0} \quad \forall (x, r)$$

where  $r_i^{s \rightarrow p}$  denotes the interface position,  $v^{s \rightarrow p}$  denotes the velocity of the interface between source (s) and product (p) phases that undergo phase transition. The step function  $\delta$ , is defined to be unity at  $r_i^{s \rightarrow p}$ . At the beginning of discharge of LFP cathode, the particle gets lithiated and hence the transformation is from  $\alpha \rightarrow \beta$ . In other words  $\alpha$  is the source and  $\beta$  the product. Consequently, subscript 'i' in the diffusivity coefficient can either be 's' or 'p' depending upon the regime of phase coexistence. General expression for interface boundary velocity is obtained by the Stefan condition based on the mass balance at the interface and is given as:

$$v^{s \rightarrow p} = \frac{dr_i^{s \rightarrow p}}{dt} = \frac{1}{(c_{eq}^p - c_{eq}^s)} \left[ D_s \frac{\partial c}{\partial r} \Big|_{r=r_i^{s \rightarrow p}(t)^-} - D_p \frac{\partial c}{\partial r} \Big|_{r=r_i^{s \rightarrow p}(t)^+} \right] \quad (9)$$

The sharp interface model imposes the following Dirichlet boundary condition at the interface

$$c = c_{eq}^p \quad \text{at} \quad r = r_i^{s \rightarrow p}(t) \quad (10)$$

The criterion for phase transformation is given as  $c \geq c_{eq}^s$ . It is to be noted that the boundary condition (Eq. (10)) that separates the two phase is not fixed in space. The interface variable  $r_i^{s \rightarrow p}(t)$ , which denotes position of the interface, evolves with time as given by Eq. (9). The set of equations required to account for phase transitions in electrode, cathode in the present case, are given by Eqs. (6)–(10). The nature of equations is kept general enough to account for forward and reverse transformation during charge/

**Table 2**  
Solid phase diffusion equations based on generalized moving boundary model.

Equation	Discharging ( $c > c_{eq}^{\alpha}$ )	Charging ( $c < c_{eq}^{\beta}$ )
Core	$[ur_i^{\alpha \rightarrow \beta}(t)]^2 \left( \frac{\partial C}{\partial t} - ur_i^{\alpha \rightarrow \beta}(t) \frac{dr_i^{\alpha \rightarrow \beta}(t)}{dt} \right) = \frac{\partial}{\partial u} \left( D_{\alpha} u \frac{\partial C}{\partial u} \right)$	$[v(R - r_i^{\beta \rightarrow \alpha}(t) + r_i^{\beta \rightarrow \alpha}(t))]^2 \left( \frac{\partial C}{\partial t} - \frac{1-u}{R - r_i^{\beta \rightarrow \alpha}(t)} \frac{dr_i^{\beta \rightarrow \alpha}(t)}{dt} \right) = \frac{\partial}{\partial v} \left( D_{\beta} \left( \frac{[v(R - r_i^{\beta \rightarrow \alpha}(t) + r_i^{\beta \rightarrow \alpha}(t))]^2 \frac{\partial C}{\partial v}}{[R - r_i^{\beta \rightarrow \alpha}(t)]^2} \right) \right)$
Shell	$[v(R - r_i^{\alpha \rightarrow \beta}(t) + r_i^{\alpha \rightarrow \beta}(t))]^2 \left( \frac{\partial C}{\partial t} - \frac{1-v}{R - r_i^{\alpha \rightarrow \beta}(t)} \frac{dr_i^{\alpha \rightarrow \beta}(t)}{dt} \right) = \frac{\partial}{\partial v} \left( D_{\beta} \left( \frac{[v(R - r_i^{\alpha \rightarrow \beta}(t) + r_i^{\alpha \rightarrow \beta}(t))]^2 \frac{\partial C}{\partial v}}{[R - r_i^{\alpha \rightarrow \beta}(t)]^2} \right) \right)$	$[ur_i^{\beta \rightarrow \alpha}(t)]^2 \left( \frac{\partial C}{\partial t} - ur_i^{\beta \rightarrow \alpha}(t) \frac{dr_i^{\beta \rightarrow \alpha}(t)}{dt} \right) = \frac{\partial}{\partial u} \left( D_{\alpha} u \frac{\partial C}{\partial u} \right)$
Core bc	$D_{\alpha} \frac{\partial C}{\partial u} \Big _{u=0} = 0, \quad C_{\alpha} _{u=1} = C_{eq}^{\alpha}$	$D_{\beta} \frac{\partial C}{\partial v} \Big _{v=0} = 0, \quad C_{\beta} _{v=1} = C_{eq}^{\beta}$
Shell bc	$C_{\beta} _{v=0} = C_{eq}^{\beta}, \quad D_{\beta} \frac{\partial C}{\partial v} \Big _{v=1} = (R - r_i^{\alpha \rightarrow \beta}(t)) \frac{dr_i^{\alpha \rightarrow \beta}(t)}{dt}$	$C_{\alpha} _{u=0} = C_{eq}^{\alpha}, \quad D_{\alpha} \frac{\partial C}{\partial u} \Big _{u=1} = \frac{D_{\beta}}{[R - r_i^{\beta \rightarrow \alpha}(t)]^2} \frac{\partial C}{\partial v} \Big _{v=0} = [C_{eq}^{\alpha} - C_{eq}^{\beta}] \frac{dr_i^{\beta \rightarrow \alpha}(t)}{dt}$
Interface movement		

**Table 3**

Geometric and material properties for LFP/C cell used in present simulations.

Parameter	Symbol	Natural graphite	Iron-phosphate
Electrode thickness [15] ( $\mu\text{m}$ )	$\delta$	50	75
Electrode porosity [15]	$\varepsilon$	0.33	0.27
Average particle radius [15]	$R$	11 $\mu\text{m}$	52 nm
Density [15] ( $\text{kg m}^{-3}$ )	$\rho$	3370	3600
Diffusion coefficient [15] (solid phase) $\text{m}^2 \text{s}^{-1}$	$D_s$	$9 \times 10^{-14}$	$8 \times 10^{-18}$
Reaction rate constant [15]	$k$	$3 \times 10^{-5}$	$3 \times 10^{-17}$
Matrix phase conductivity [15] ( $\text{S m}^{-1}$ )	$\sigma_s$	100	$5 \times 10^{-3}$
Maximum concentration [15] ( $\text{mol m}^{-3}$ )	$c_s^{\text{max}}$	27,760	20,950
Parameter		Value	
Separator thickness [15] ( $\mu\text{m}$ )	$l_s$	25	
Separator porosity [15]	$\varepsilon_{\text{sep}}$	0.55	
Separator density [15] ( $\text{kg m}^{-3}$ )	$\rho_{\text{sep}}$	900	
Electrolyte density [15] ( $\text{kg m}^{-3}$ )	$k_1$	1200	
Equilibrium concentration for $\alpha$ [16]	$C_{eq}^{\alpha}$	$0.048 c_{\text{max}}$	
Equilibrium concentration for $\beta$ [16]	$C_{eq}^{\beta}$	$0.8920 c_{\text{max}}$	

discharge or simultaneous charge–discharge. The specific details of these equations (Eqs. (6)–(10)) and the coupling with Eqs. (1)–(5) using the pseudo 2-D approach is discussed in the next section. For electrodes without phase transitions, however (anode in the present case) Eq. (6) without the interface movement term along with boundary and initial condition as in Eqs. (7) and (8) respectively characterizes the diffusion process.

#### 4. Path dependent model for LFP/C cell and numerical implementation

Interface coupled diffusion problem as described in the earlier section (Eqs. (6)–(10)) falls under the general class of inverse mathematical problem called Stefan [39] problem. These kinds of problems arise in several phase transition phenomenon like solidification of molten metal [40], crystal growth [38] and martensitic transformation [41] during steel forming. In order to numerically solve Eqs. (6)–(10) several methods and algorithms [13,39] are proposed. These methods can be classified as fixed mesh method and moving mesh method. Moving mesh method [42] uses ALE (Arbitrary Lagrangian–Eulerian) approach and allows for motion of the boundary. The mesh motion is defined in Eulerian coordinates and is independent of motion of the material, defined in Lagrangian coordinates. This method, however, requires sophisticated solvers and smoothing techniques and hence is computationally cumbersome. Fixed grid methods on the contrary [13–15], use the concept of similarity transformation to convert the moving boundary problem to fixed coordinates. One such method, known as Landau transformation [43], is used in the solution of electrochemical model for lithium ion cells and is adapted in this work.

In context of LFP, using Landau transformation two new static position variables  $u$  and  $v$  are introduced, one for each phase. During discharge when  $\alpha$  is the source and  $\beta$  is product, the domain of spherical particle  $\Omega$  can be considered to be constituted of  $\Omega_{\alpha} \cup \Omega_{\beta}$  where  $\Omega_{\alpha} \in [0, r_i^{\alpha \rightarrow \beta}(t)]$  and  $\Omega_{\beta} \in [r_i^{\alpha \rightarrow \beta}(t), R]$ . Using the spatial variable  $u$  which is given as  $u = r/r_i^{\alpha \rightarrow \beta}(t)$ , fixed coordinate equation for diffusion in  $\alpha$  phase or the core is obtained. Similarly using ‘ $v$ ’ defined as  $v = (R - r_i^{\alpha \rightarrow \beta}(t))/(R - r_i^{\alpha \rightarrow \beta}(t))$ , the corresponding fixed domain equation for diffusive transport in the shell is obtained. The transport equations during charging can also be



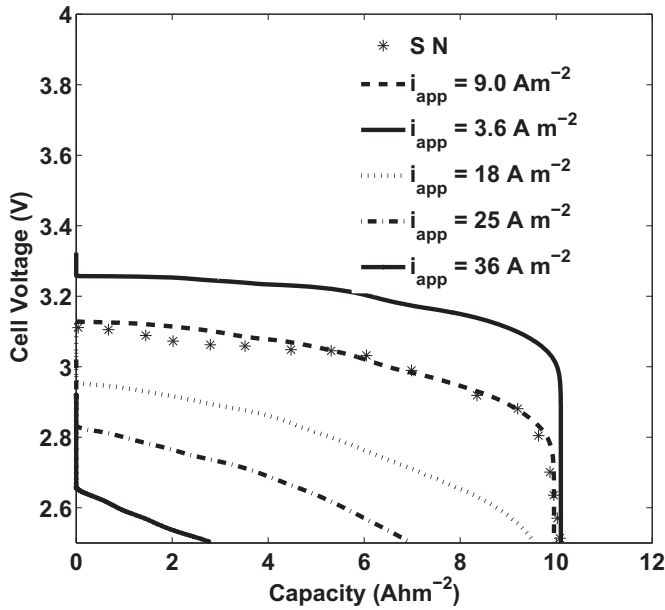


**Fig. 3.** Voltage vs capacity curve prediction for different current densities using the discharge model. Also comparison of present approach with Srinivasan and Newman [15] at  $9 \text{ A m}^{-2}$  is shown. Result from Srinivasan and Newman is marked by legend 'S N'.

obtained using similar transformations. For continuous charging after discharging (Fig. 2), the interface formed at the end of discharge will define the boundary condition for concentration (Eq. (10)). This serves as the initial condition for charging, when new interface ( $r_i^{\beta \rightarrow \alpha}$ ) evolves due to  $\alpha$  phase formation. In order to illustrate this point a schematic of charging an incompletely discharged spherical particle is shown in Fig. 2. The figure shows formation of multiple cores and shells but it is important to consider that only the outer shell of  $\alpha$  phase will be active, and hence only  $r_i^{\beta \rightarrow \alpha}$  will govern the mass transfer. This implies tracking of movement of a single interface. On the contrary, if both the interface variables ( $r_i^{\alpha \rightarrow \beta}$  and  $r_i^{\beta \rightarrow \alpha}$ ) were used to track the dynamics of phase transition, the book keeping becomes complicated, eventually rendering the formalism untenable for cyclic applications.

Using this coordinate transformation the equations that are specific to discharge and charge that evolve out of the general framework (Eqs. (6)–(10)) are listed in Table 2. Although the number of equations increases due to this transformation, the formalism is numerically less intensive as the domain does not change with time and hence can be adapted to simulate charge–discharge cycles. The complete numerical solution is obtained by combining the equations given in Table 2 with the porous electrode model (Eqs. (1)–(5)) and is solved using a Pseudo 2-D [32–36] approach.

Numerical implementation in a multi-physics environment of COMSOL [44] is obtained by suitably modifying the available lithium ion cell model to incorporate multi-phase coexistence. This is achieved by coupling the 1-D lithium ion cell model with the 2-D solid phase diffusion model along with the interface movement equation. Implicit time dependent solver with BDF (Backward differentiation formulas) for time marching is chosen with an absolute tolerance of  $1 \times 10^{-3}$  and relative tolerance of  $1 \times 10^{-2}$ . Initial numerical studies show that these values for the tolerances are adequate to achieve the desired numerical accuracy with acceptable computation times. To obtain the numerical solution at each time step a solver that suitably conditions the sparse system and optimally allocates the memory for a parallel computing

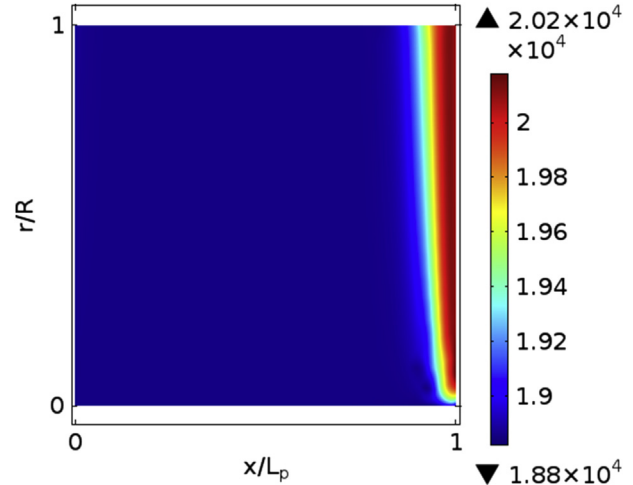


**Fig. 4.** Distribution of concentration over pseudo 2D domain of positive electrode at  $t = 3000 \text{ s}$  for applied discharge current of  $3.6 \text{ A m}^{-2}$ .

architecture (MULTifrontal Massively Parallel sparse direct Solver, MUMPS) is used. Further, a Newton–Raphson based technique is used to obtain solution for the fully coupled multi-physics PDEs.

## 5. Results and discussion

The generalized moving boundary problem developed in the earlier section is used to simulate the response of LFP/C cells under various scenarios. In this section, the details of these scenarios are presented, geometric and material parameters that are used in the simulations are listed in Table 3. Srinivasan and Newman [15] and Thorat [25] report the equilibrium potential for anode and cathode respectively. Details of these potentials are given in Appendix A, along with the electrolyte parameters. Overview of the case studies discussed in this section is as follows:

- 1) Proposed numerical implementation is validated by comparing model predictions with the shrinking core [15] model for discharge.
- 2) Generalized moving boundary model with diffusion in  $\alpha$  phase is used to simulate the discharge and charge response for various current rates. Effect of diffusion in  $\alpha$  phase is illustrated using the spatial and temporal concentration profile in the positive electrode.
- 3) Path dependent response is simulated for a charge–discharge cycle. This simulation tests the applicability of the proposed approach under realistic load conditions, in addition to analyzing path dependent asymmetric charge–discharge of LFP/C cells.
- 4) Parametric study is conducted to assess the applicability of present approach as a potential design tool.

Detailed outcomes of the individual case studies are discussed in the following subsections.

### 5.1. Model validation

In this section the model is validated by comparing with results reported by Srinivasan and Newman [15] for the discharge curve. It can be seen from Fig. 3 that the model compares well with the published results for an applied constant current of  $9 \text{ A m}^{-2}$ . Discharge curve is simulated for a range of current densities from  $3.6 \text{ A m}^{-2}$  to  $36 \text{ A m}^{-2}$ . Model outputs for different current densities

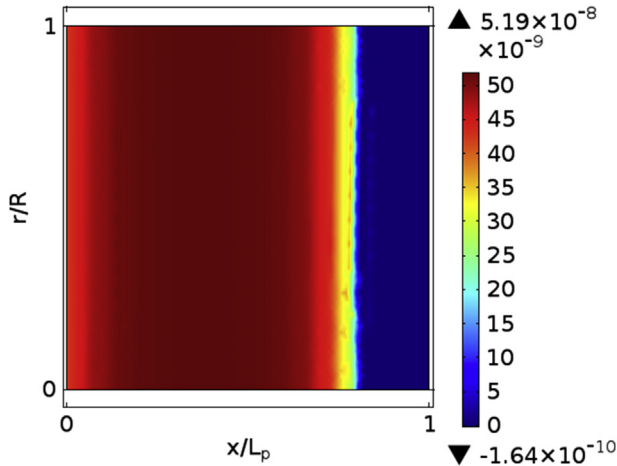


Fig. 5. Distribution of interface movement over pseudo 2D domain of positive electrode at  $t = 3000$  s for discharge current of  $3.6 \text{ A m}^{-2}$ .

are also seen in Fig. 3. The results show expected dependence on increasing current, i.e. drop in end capacity due to lower utilization of electrode particles; decrease in mid-plateau potential due to higher Ohmic losses and increase in slope of the mid-plateau region [15] due to higher transport losses.

The proposed model can be used to study the spatial distribution and evolution of Li concentration in the LFP electrode. The distribution of concentration in particles along the thickness of positive electrode, over the pseudo 2-D domain at  $t = 3000$  s is shown in the surface plot, Fig. 4. In Fig. 4 and in all subsequent surface plots of the pseudo 2D domain, the  $x$  axis denotes the thickness of the electrode, and the  $y$  axis the radius of the particle. It may be noted here that  $x = 0$  represents the separator end and  $x = L_p$  represents the current collector end of electrode. It is observed (Fig. 4) that though diffusion is modeled to propagate in radial or normal direction at the particle scale, the concentration front propagates in the tangential direction. This observation is in good accord with experimental [22,23] results for LFP. Moving one step further one can also see that phase interface variable  $r_i^{\alpha \rightarrow \beta}$  changes from almost zero at the cathode current collector end to its initial value ( $=0.99 R$ ) at the separator end as shown in Fig. 5. Value of  $r_i^{\alpha \rightarrow \beta}$  close to zero signifies interface reaching the center of the particle.

It is interesting to see in Figs. 4, 5 that there is higher concentration and hence a higher utilization at the current collector end in

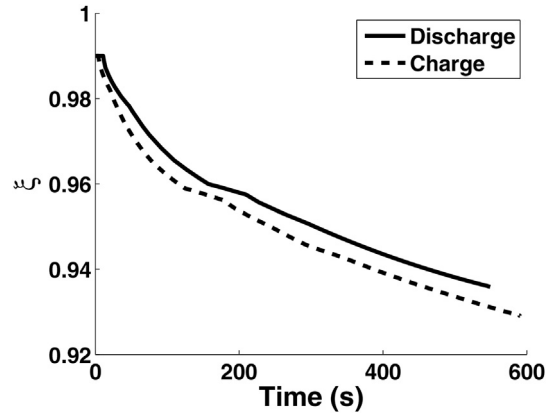


Fig. 7. Comparison of evolution of interface variable  $\xi$  for constant current charge and discharge of  $54 \text{ A m}^{-2}$ .

comparison to the separator end. This feature is specific to LFP electrodes, as an opposite trend is observed [45] for other electrodes. The reason for the tangential propagation of the concentration front as well as the higher utilization at the collector end can be ascribed to the lower electrical conductivity of LFP particle. A higher utilization implies a higher rate of surface reaction. An electrode with a higher electrical conductivity leads to a design case where the electrolyte conductivity is limiting. This eventually results in a higher reaction flux at the separator end where the ions are in abundance. In the case of a porous LFP electrode however, the controlling process is electrical conductivity, and hence the trend is reverse. Implications of this feature in optimal cell design needs to be investigated. It is clear however, that any increase in conductivity will enhance the uniformity in exchange current density and hence the utilization. This assertion is quantitatively attested by means of parametric study in Section 5.4.3. The focus of this section is on validating a discharge model for cells with phase change electrodes. Further, diffusion in  $\alpha$  phase is required to describe charge–discharge response as discussed in Sections 3 and 4. Results from numerical simulation of the general charge–discharge model are discussed in subsequent sections.

## 5.2. The charge–discharge response of LFP/C cells

In this section, the results of the generalized moving boundary model to represent discharge and charge behavior are presented. It

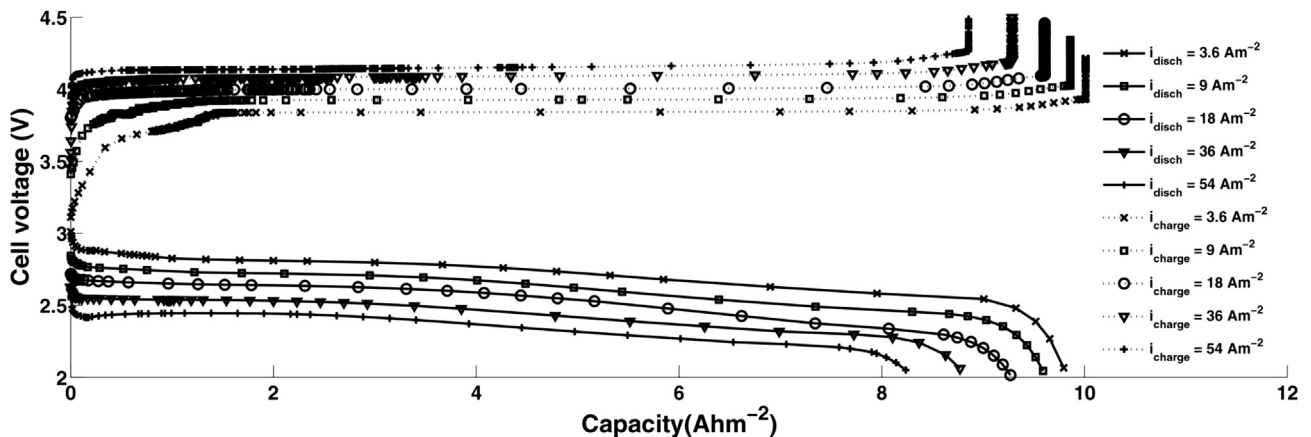


Fig. 6. Voltage vs capacity curve for charging and discharging for different current densities.

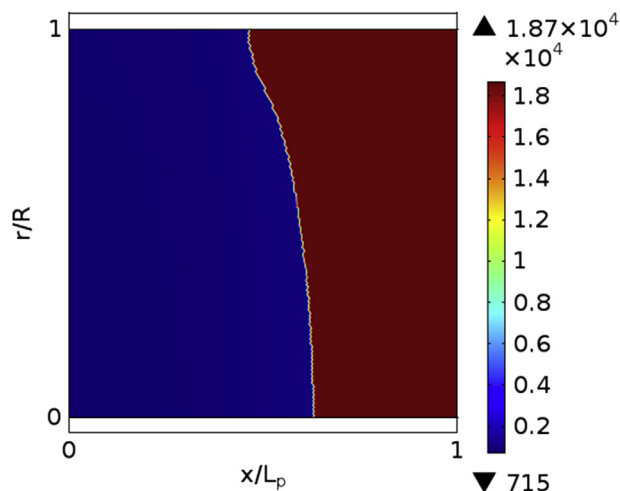


Fig. 8. Distribution of concentration over pseudo 2D domain of positive electrode during discharge.

may be noted that while charging LFP electrodes, lithium deficient  $\alpha$  phase forms the shell in contrast to discharge. In the present simulation, for diffusivities of  $\alpha$  and  $\beta$  phase, experimental values reported by Safari and Delacourt [26],  $1.184 \times 10^{-18} \text{ m}^2 \text{ s}^{-1}$  and  $3.907 \times 10^{-19} \text{ m}^2 \text{ s}^{-1}$  respectively are used. Detailed parametric dependence on diffusivity is presented in later sections. The cell voltage against capacity (defined as the product of current density and the time of charge/discharge) for charge and discharge at various current densities is shown in Fig. 6. Charge voltage profile exhibits similar trends as discharge: increase in initial voltage, decrease in end capacity and increase in mid-plateau slope with increase in current density. Importantly, on comparing voltage profiles of charge and discharge (Fig. 6) much higher utilization is seen during charge in comparison to discharge at higher current densities. At lower current densities the difference of utilization between charge and discharge is lesser. This result is in accord with experimental observations by Srinivasan and Newman [29], where it is reported that the decrease in utilization (or end capacity) with increase in current density is smaller during charge as compared to discharge. Hence, it is evident that this model can be used to represent and assess the asymmetry in the charge and discharge response of LFP/C cells.

It may be mentioned that although discharge and charge voltages show asymmetric behavior (Fig. 6), these results are obtained using the same  $U_{eq}$ , and hence the asymmetry is of transport origin (Srinivasan and Newman [29]). A further cause of asymmetry could be due to difference in the  $c_{eq}^\alpha$  and  $c_{eq}^\beta$  values that initiate phase transformation from  $\alpha$  to  $\beta$  phase and vice-versa. These concentrations correspond to different equilibrium voltages ( $U_{eq}$ ), and over-potentials ( $\phi_s - \phi_e - U_{eq}$ ) resulting in different rates of charge transfer and diffusion processes between the lithium rich and lithium poor phases. It can be seen in Fig. 6 that at low rates of charge and discharge the voltage capacity curve is nearly symmetric, and as the rate of discharge or charge increases the asymmetry increases. In order to explain this observation, the interface movement variable during  $\alpha \rightarrow \beta$  ( $\xi = r_i^{\alpha \rightarrow \beta}/R$ ) and  $\beta \rightarrow \alpha$  ( $\xi = r_i^{\beta \rightarrow \alpha}/R$ ) transitions, normalized with radius of particle, is plotted at a high current of  $54 \text{ A m}^{-2}$  in Fig. 7. As seen in Fig. 7 the velocity of the interface is different between charge and discharge, owing to difference in diffusivity of  $\alpha$  and  $\beta$  phases. Importantly the onset of phase transformation is also different due to difference in diffusivity and equilibrium concentrations.

Subsequently the effect of modeling  $\alpha$  phase diffusion is investigated by assessing the concentration distribution in the positive

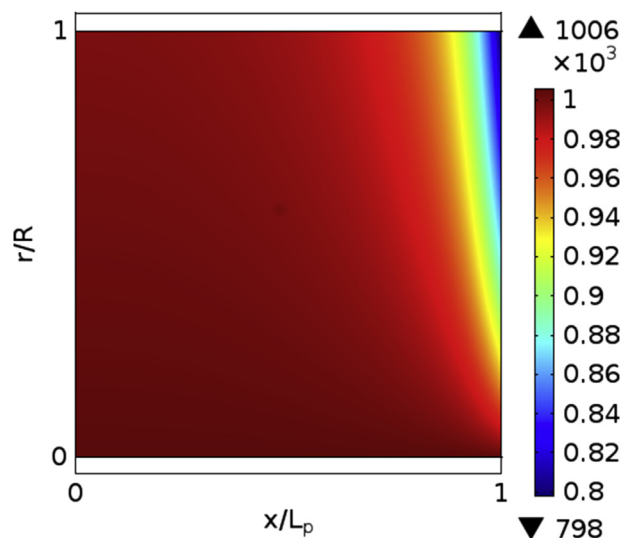


Fig. 9. Distribution of concentration over pseudo 2D domain of positive electrode at end of pulse I.

electrode during discharge as shown in the surface plot, Fig. 8. In the snapshot shown in Fig. 8, the concentrations of both the phases are separated by a front that eventually propagates from the correct collector to the separator end. Thus the propagation of the concentration front (in  $x$  direction) is tangential to the direction of lithium intercalation, as the latter occurs in the  $y$  (radial) direction into the particles. Thus, this surface plot shows the tangential phase front movement as well as the separation of the  $\alpha$  and  $\beta$  phases. In a recent work by Fergusson and Bazant [46], this phenomenon observed in LFP particles is highlighted well and the same is captured through non-equilibrium thermodynamics based phase field theory. In comparison, the present approach uses a computationally simpler framework of porous electrode theory to arrive at similar conclusions. It is to be mentioned that low solid diffusivity of LFP particle promotes the tangential phase front propagation during charge–discharge process.

It can be observed from Fig. 8 that the two phase coexistence causes higher concentration gradients due to the difference between the equilibrium concentrations of the two phases. It is reported [47] that high concentration gradients due to phase separation lead to build up of high stress gradients. These stress gradients induced during intercalation process result in increased crack formation [48] in electrodes. The stress induced cracks, in turn, lead to poor electric contact and/or capacity fade due to active Li loss by fragmentation or isolation of electrode particles and eventually to cyclic instability. Thus the stress in-homogeneities in due course of intercalation cycles can be detrimental from material mechanical fatigue point of view. Such scenarios can be averted by choosing an operating window in predominantly one phase region, or tailoring the materials for a narrower equilibrium concentration window or increasing the phase transformation sites. The proposed approach can be used to model such aging processes on incorporation of suitable coupled stress effects.

### 5.3. Path dependent behavior during charge–discharge pulse

In the experimental study by Srinivasan and Newman [29] and Roscher [49] the asymmetric behavior of LFP cathode between charge and discharge is summarized. It is concluded that at the same current density LFP electrode shows higher utilization during charge. This in turn confirms the asymmetric utilization between



charge and discharge. The path dependence in LFP system, however, arises when the particles are not fully charged or discharged – if the phase transformation in any one direction is not fully completed. For instance, a fully charged particle (stage I of Fig. 1) discharged till stage III and charged again shows a different behavior if similar state of charge is obtained using a different path. Such path dependence is characteristic of materials that exhibit phase transition.

In this section, using the generalized moving boundary approach, the path dependence response is investigated. It is to be noted that the differences in transport and kinetic parameters during charging and discharging is not considered in this study. It is interesting to investigate if the path dependent response is exhibited even without this information. In this subsection complete voltage profile for a continuous charge–discharge cycle is simulated for following the two types of pulse inputs:

- I. Constant current 1-C discharge for 9000 s followed by rest of 5000 s and charge at 1-C for 9000 s followed by rest.
- II. Constant current 7-C discharge for 500 s followed by rest of 900 s and then charge at 7-C for 600 s.

Pulse I is chosen to analyze the phase separation and path dependence. Pulse II shows the effects of rapid charging and discharging. Pulse II is studied to demonstrate efficacy of present approach under realistic drive cycles. Concentration distribution across the positive electrode under pulse I during discharge is shown in Fig. 8, and at the end of the pulse in Fig. 9. The path dependent behavior of phase change electrode as discussed in Fig. 1 is quantitatively obtained in Figs. 8, 9, where the successive occurrence and de-occurrence of phase separation are clearly seen. Temporal evolution of concentration at the surface of positive electrode particles located at current collector end is shown in Fig. 10. The discontinuous evolution of concentration during  $\alpha \rightarrow \beta$  and  $\beta \rightarrow \alpha$  phase transformation during discharging and charging of LFP particle is demonstrated in Fig. 10. The initial concentration evolution during the  $\alpha \rightarrow \beta$  transition is shown in the inset of the figure. The asymmetric nature of utilization in LFP cell during continuous discharge–charge regime of pulse I is also seen in Fig. 10. Further, some amount of lithium (denoted as  $\Delta C$  in Fig. 10) remains unused after one charge–discharge cycle. This unused

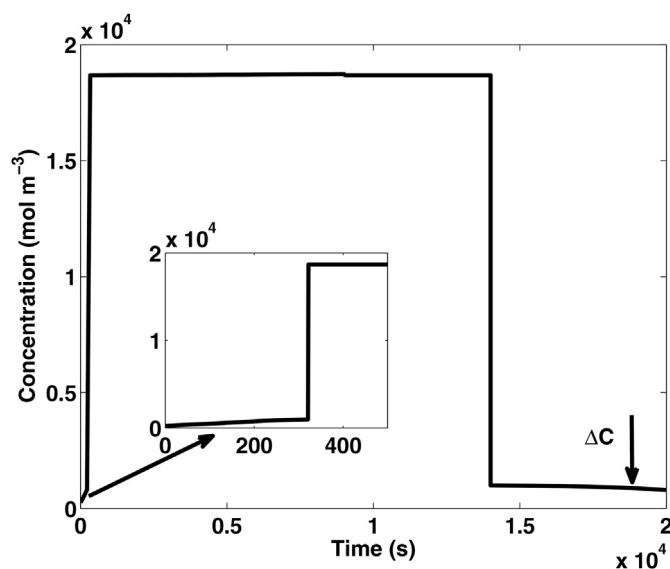


Fig. 10. Concentration vs time profile at particle surface located at current collector end, showing the difference at the end and start of pulse I.

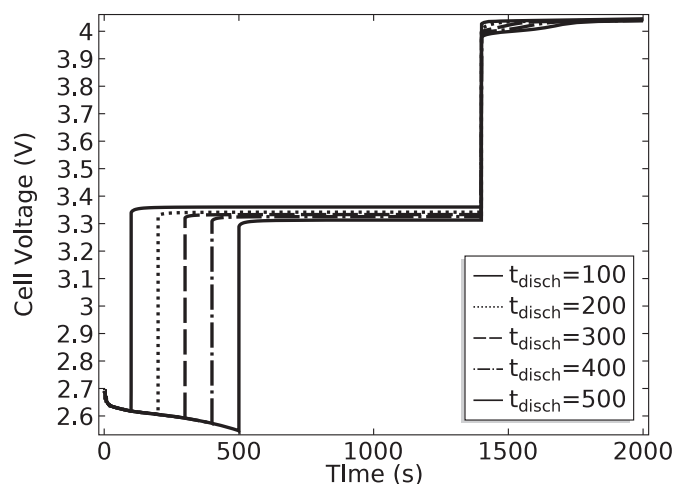


Fig. 11. Voltage vs time during discharge and charge for constant current of  $25 \text{ A m}^{-2}$  (pulse II).

lithium accounts for the observed phenomenon of capacity loss in LFP cells. One can also see that the concentration at the end of charge is not uniform as shown in Fig. 9. Interestingly recent results on X-ray absorption spectroscopy (XAS) by Ouvrard et al. [50] also show such heterogeneity in LFP particles. A manifestation of such heterogeneity is a reduction in amount of active  $\text{Li}^+$  ion during intercalation cycle of the cell which eventually [51–54] leads to capacity loss. Such a capacity loss, as it does not involve irreversible side reactions or structural damage, can be recovered by long time relaxations.

In order to further demonstrate the efficacy of the proposed approach in bringing out the path dependency, simulation under pulse II is performed with different extents of discharge as seen in Fig. 11. The protocol starts from a fully charged cell, the varying extents of discharge corresponds to a difference in end of discharge SOC of 0.2 between the pulses. The corresponding voltage during the subsequent charging pulse is shown in Fig. 11, and a detailed view is given in Fig. 12. It can be gleaned from the results that varying extents of discharge alters the subsequent charging response. It needs to be mentioned that this behavior is observed irrespective of the fact that the end of discharges correspond to

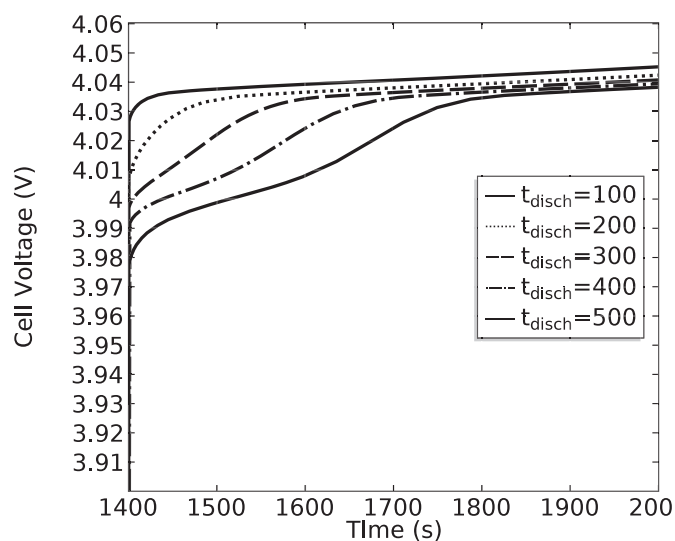


Fig. 12. Voltage vs time highlighting the effect of different extents of discharge on the charging profile.

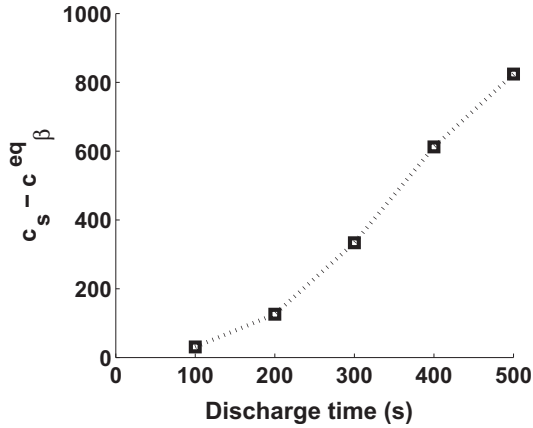


Fig. 13. Difference in surface concentration vs time at current collector end of cathode for different discharge times.

SOCs where  $U_{eq}$  is almost constant. The cause of this feature, thus, can be ascribed to difference in the concentration distribution in the positive electrode that would respond differently between discharge and charge. A reversal of current loading from discharge to charge would induce a reversal of phase transformation, resulting in differences in the concentration profile. Specifically, on discharging for longer times, the surface concentration of cathode particles at the end of discharge are farther away from  $c_{eq}^{\beta}$  (Fig. 13). During the subsequent charging, these values equilibrate back to  $c_{eq}^{\beta}$  before a shell of  $\alpha$  phase is formed. Thus, the charging profile in Fig. 12 varies according to the preceding extent of discharge. It can be also seen from Fig. 12 that the time to achieve the constant voltage region (which corresponds to the two phase coexistence) is longer, if the extent of discharge is larger. Thus the path dependency occurs due to varying relaxation mechanisms corresponding to the operating history. Such observations due to path dependency in the present numerical study corroborate well with the trends observed experimentally [48] on LFP based cells. The magnitude of voltage difference observed for different instants of discharging in the present simulations is in accord with experimental observations. Further, it may be reiterated here that the voltage difference is obtained with the same values of diffusivity for both the solid phases; the impact is expected to become more significant with incorporation of such change. Sensitivity of

diffusivity on the path dependence will be studied in a later section. As discussed by Ramana [31] and Roscher and Sauer [55], another reason of path dependency in LFP cathode is due to inherent hysteresis in open circuit voltage during forward and reverse transformation. Incorporation of such hysteretic OCV will accentuate the asymmetry in the charge–discharge response.

#### 5.4. Parametric study: assessment of cell design

In this subsection results of parametric sensitivity on cell performance are presented. Aim of this study is to investigate the correlation of the extent of phase transformation with macroscopic cell response. The studies in this section suggest that, useful design conclusion can be derived using a parametric sensitivity analysis. In this section, effect of the following three important parameters is studied:

1. Solid phase diffusivity
2. Radius of particle
3. Electronic conductivity

The above choice of parameters is inspired from various research findings that have identified the two important deficiencies of LFP electrode as higher transport losses and low rate capability. To overcome these deficiencies the natural choice is to increase the diffusivity, decrease the particle radius or increase electronic conductivity. Analysis in this section aims at identifying the critical parameters that can enhance the cell performance.

##### 5.4.1. Effect of solid phase diffusivity on discharge behavior

Diffusivity values of both the  $\alpha$  &  $\beta$  phase are set to be equal and is varied from  $8 \times 10^{-16}$  to  $8 \times 10^{-20} \text{ m}^2 \text{ s}^{-1}$  and the discharge response for a constant applied current of  $3.6 \text{ A m}^{-2}$  is shown in Fig. 14. The corresponding interface movement is shown in Fig. 15. It is seen that higher diffusivity results in faster interface movement and higher capacity (Figs. 14 and 15). Eq. (9) shows that solid phase diffusivity is directly proportional to interface velocity. For the lowest value of diffusivity, steeper concentration gradients result in quick saturation of the surface concentration of the cathode particles which in turn result in drop in the cell voltage (Fig. 14). These results in a scenario where particles of the positive electrode are not utilized completely (Fig. 14). This study suggests that the optimal value of diffusivity would be  $8 \times 10^{-18} \text{ m}^2 \text{ s}^{-1}$ , as increasing diffusivity beyond this value enhances the voltage and capacity

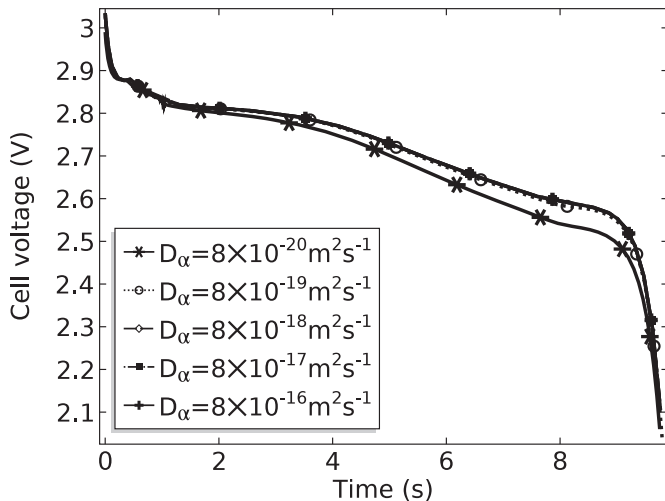


Fig. 14. Discharge curve for different values of solid phase diffusivity for constant current discharge of  $3.6 \text{ A m}^{-2}$ .

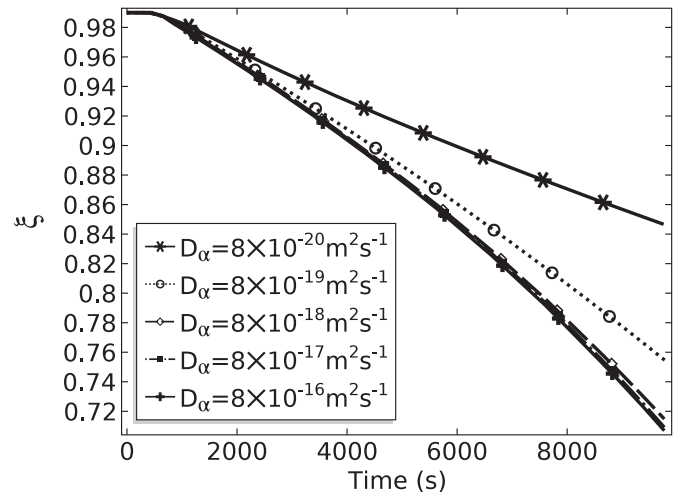
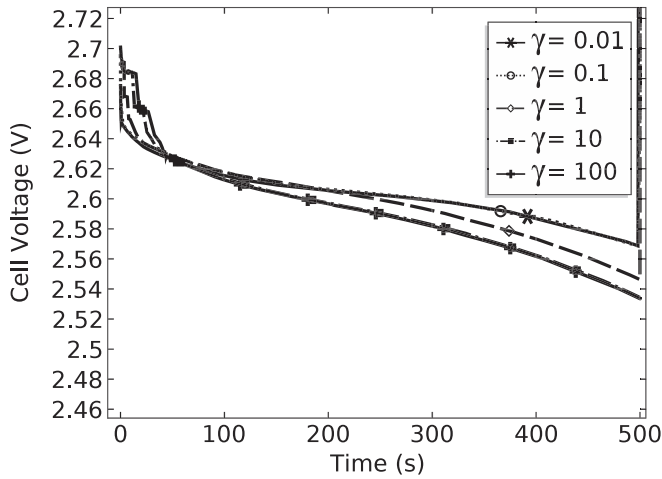


Fig. 15. Evolution of normalized interface variable  $\xi$  for different values of solid phase diffusivity at  $3.6 \text{ A m}^{-2}$ .



**Fig. 16.** Voltage vs time profile during discharge of pulse II to highlight the effect of different diffusivities of  $\alpha$  phase.

response marginally (Fig. 14). Interface movement (Fig. 15) also shows similar trends beyond the value of  $8 \times 10^{-18} \text{ m}^2 \text{ s}^{-1}$  for diffusivity.

#### 5.4.2. Effect of solid phase diffusivity on path dependence during continuous discharge and charge pulse

This case study highlights the importance of solid phase diffusivity on the path dependence of cell response. In order to examine this effect, simulation under pulse II (described in Subsection 5.3) is performed for different diffusivities of  $\alpha$  phase while maintaining a constant diffusivity of the  $\beta$  phase. The cell voltage variation with capacity is shown in Fig. 16 for discharge at different values of the diffusivity ratio  $\gamma$ , defined as  $\gamma = D_\alpha/D_\beta$ . During discharge, the system is predominantly in the two phase coexistence region, and as the  $\beta$  phase evolves, the mass transport is governed by the interface movement. The interface movement is governed by the difference in diffusion flux of the two phases (Eq. (9)), and is slower for higher diffusivity of  $\alpha$  phase. This in turn results in higher concentration gradients in the shell ( $\beta$  phase) and higher voltage drop during discharge. Upon successive charging (Fig. 17) however, the system is predominantly in the single phase ( $\beta$ ) region and the expected dependence on diffusivity is observed. Thus it can be seen

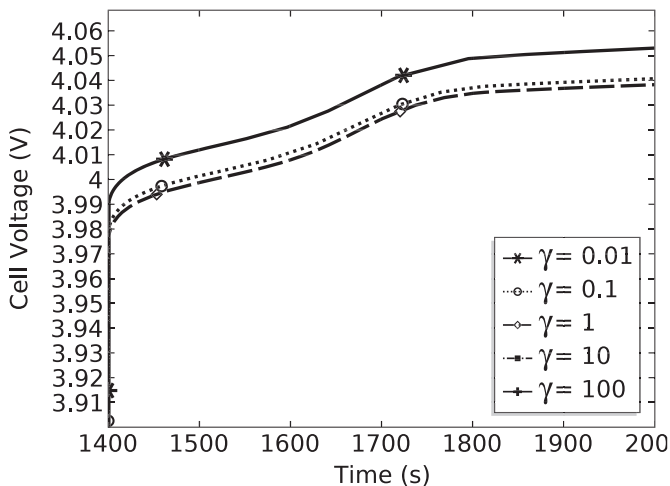


**Fig. 17.** Voltage vs time profile during charge of pulse II to highlight the effect of different diffusivities of  $\alpha$  phase.

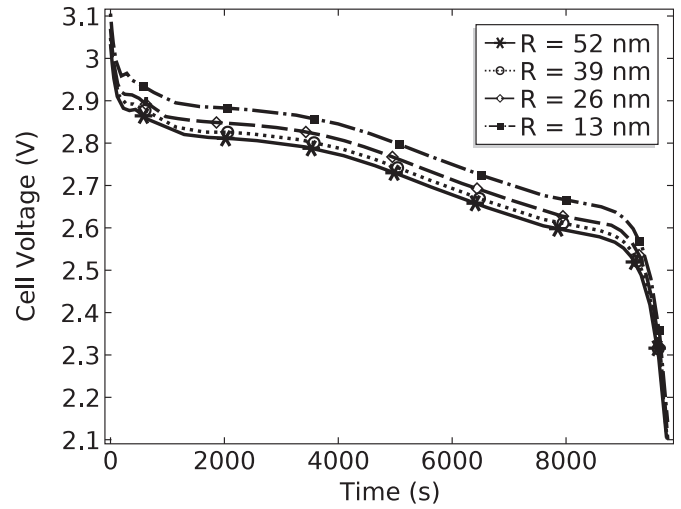


**Fig. 18.** Discharge curve for different particle radii at constant current of  $3.6 \text{ A m}^{-2}$ .

that multi-phase coexistence brings about the effect of diffusivities of both the solid phases on the cell voltage profile.

#### 5.4.3. Effect of particle radius

One of the suggested ways to improve the rate capability or transport limitation in LFP electrodes is to reduce the particle size. The discharge curve at a current density of  $3.6 \text{ A m}^{-2}$  for particle radius decreasing from 52 nm to 13 nm is shown in Fig. 18. It can be seen from Fig. 18 that a decrease in particle radius decreases the diffusional resistances, and for the same applied current, results in higher discharge voltage. The discharge capacity, however, increases marginally on reducing the particle radius to 13 nm, as seen in Fig. 18. The interface movement at these particle radii (Fig. 19) also does not show any significant differences. Interestingly recent experimental studies by Chueh et al. [56] confirms the findings of present simulation results wherein it is reported that reducing particle size may not be useful, due to lower diffusion coefficient in LFP. Any further enhancement could only be achieved by inducing the onset of the phase transformation of a larger number of particles. It may also be mentioned that particle radius reduction does not enhance the cell performance during charging either.

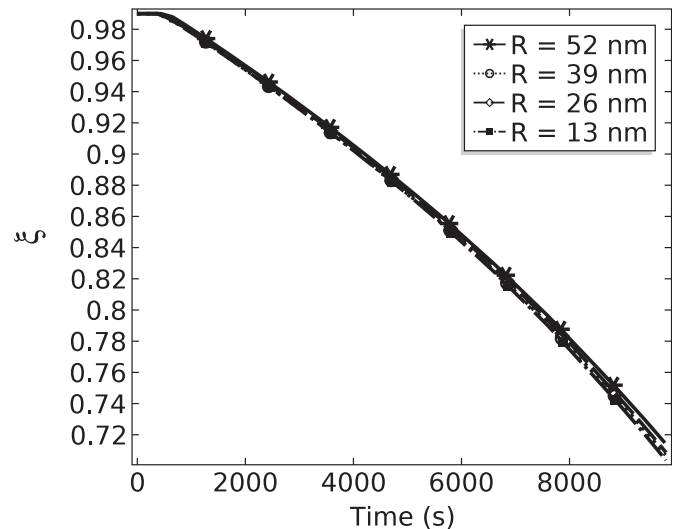


**Fig. 19.** Evolution of interface variable  $\xi$  for different particle radii at constant current of  $3.6 \text{ A m}^{-2}$ .

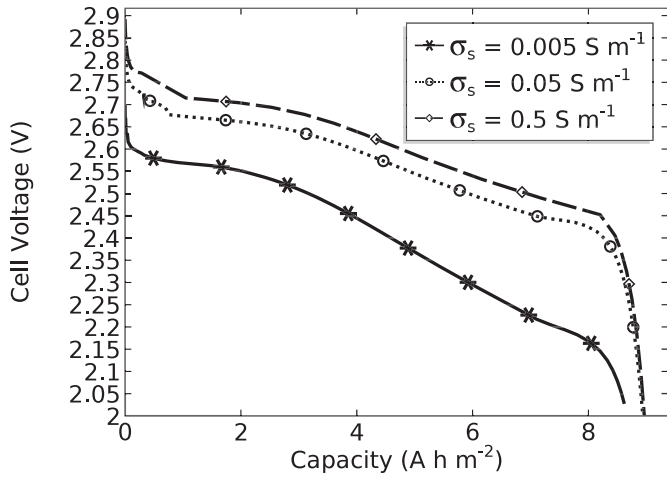


Fig. 20. Discharge curve for different values of electrical conductivity at constant current of  $36 \text{ A m}^{-2}$ .

#### 5.4.4. Effect of electronic conductivity

As mentioned earlier, one of the important limitations of LFP electrodes is the low electronic conductivity. This causes higher Ohmic drops in the electrodes and low rate capability leading to reduced active material utilization. The present case study aims at elucidating the effect of electronic conductivity on cell voltage and discharge capacity. To highlight this effect, discharge at a higher constant current density of  $36 \text{ A m}^{-2}$  is performed for three different values of conductivity varying in multiples of 1, 10 and 100 from the base value of  $5 \times 10^{-3} \text{ S m}^{-1}$ . As seen in Fig. 20 the corresponding discharge curve shows enhanced performance with higher discharge voltage and increased utilization with increase in conductivity. Increase in voltage is due to reduced Ohmic drop and increase in utilization (or end capacity) is due to lower transport losses. It is also observed from the concentration distribution at the electrode level (figure not shown) that reduction in Ohmic drop increases the reaction flux at the particle surface. This results in the concentration front emanating from both the collector and the separator end of the electrode leading to higher utilization. It is to be noted that further increasing the conductivity from  $0.05 \text{ S m}^{-1}$  to  $0.5 \text{ S m}^{-1}$  enhances the performance marginally (Fig. 20) and hence an optimal choice of conductivity is  $0.05 \text{ S m}^{-1}$  for better cell design. It can be concluded in this section that out of the three parameters studied conductivity has the dominant effect in improving the performance of LFP based cells.

## 6. Summary and conclusion

In this work a generalized moving boundary framework for lithium ion cells with electrodes that exhibit phase transition is proposed. This framework is used to develop electrochemical model based on pseudo 2-D approach of porous electrode theory. Using suitable coordinate transformation the moving domain problem is translated in to an equivalent fixed coordinate system. Suitable path dependent algorithm is devised to model the electrochemical response under continuous charge and discharge cycle. Numerical simulations show efficacy of the present approach in suitably capturing the underlying electrochemical processes in LFP/C cells namely, tangential front propagation, phase separation, charge–discharge asymmetry and path dependent response. The concentration front propagates tangentially in due course of discharge owing to lower diffusivity and electrical conductivity of LFP electrodes. Generalized core

shell model ascribes sharp interface formation between the two solid phases of LFP which adequately captures the phase separation. Phase separation in LFP is a very important physical phenomenon as it causes steep concentration gradients. These gradients result in high stress generation and are tantamount to mechanical fatigue. Charge–discharge study at various currents predicts asymmetry in cell utilization, and especially at higher rates it is found that utilization is higher during charge in comparison to discharge. This prediction of lower utilization at higher current density during discharge as compared to charge corroborates well with the experimental results. Comparison of interface movement during charge and discharge confirms the difference in utilization and ascribes this asymmetry to be of transport origin. Another important feature of the proposed generalized framework lies in its ability to model the path dependent response. Robustness of present numerical implementation is shown by predicting the response for both high and low rate charge–discharge pulse protocol. Also it is shown that the charging voltage profile depends on the extent of preceding discharge, resulting in the path dependent response of phase change LFP material. Parametric sensitivity studies suggest that among the important properties of LFP (diffusivity, particle radius and electronic conductivity) increase in conductivity enhances cell performance significantly. A higher electrical conductivity enhances the phase transformation resulting in to improved cell performance.

The generalized moving boundary framework proposed here can be coupled with energy balance equations to develop a non-isothermal model to facilitate thermal management studies. Assessment of carbon coating or solid-solution doping and other enhancement features can be incorporated. Furthermore the model can be coupled to mechanical momentum balance equations to predict stress gradient due in a phase change electrode material to develop fatigue models to study battery aging. Some of these extensions are in progress.

## Appendix A

This appendix enlists the equilibrium potential for LFP cathode which is given in Ref. [25] as:

$$U = 2.56742 + 57.69 \left( 1 - \tanh \left( 100 \frac{c}{c_{\max}} + 2.9163927 \right) \right) + 0.442953 \tanh^{-1} \left( -65.41928 \frac{c}{c_{\max}} + 64.89741 \right) + 0.097237 \tanh^{-1} \left( -160.9058 \frac{c}{c_{\max}} + 154.59 \right)$$

Similarly the equilibrium potential for graphitic anode is adopted from Ref. [16] and is given in terms of electrode state of charge ( $x$ ) as:

$$U(x) = 0.124 + 1.5 \exp(-70x) - 0.0351 \tanh \left( \frac{x - 0.0286}{0.083} \right) - 0.0045 \tanh \left( \frac{x - 0.9}{0.119} \right) - 0.035 \tanh \left( \frac{x - 0.99}{0.05} \right) - 0.0147 \tanh \left( \frac{x - 0.5}{0.034} \right) - 0.102 \tanh \left( \frac{x - 0.194}{0.142} \right) - 0.022 \tanh \left( \frac{x - 0.98}{0.0164} \right) - 0.011 \tanh \left( \frac{x - 0.124}{0.0226} \right) + 0.0155 \tanh \left( \frac{x - 0.105}{0.029} \right)$$

The electrolyte properties – diffusivity and conductivity [15], used in the present study are given respectively as:



$$D = 5.34 \times 10^{-10} \exp\left(-1.565 \times 10^{-4} c_e\right) \text{m}^2 \text{s}^{-1}$$

$$\kappa_e = 0.0911 + 1.901 \times 10^{-3} c_e - 1.052 \times 10^{-6} c_e + 0.1554 \times 10^{-9} c_e \text{S m}^{-1}$$

where  $c_e$  is the electrolyte concentration  $\text{mol m}^{-3}$ .

#### List of symbols

$a_s$	Active surface area per electrode unit volume for electron transfer reactions, $\text{m}^{-1}$
Brug	Bruggeman coefficient
$c$	lithium concentration, $\text{mol m}^{-3}$
$c_s$	lithium concentration at the surface of electrode, $\text{mol m}^{-3}$
$c_0$	initial lithium concentration, $\text{mol m}^{-3}$
$c_e$	$\text{Li}^+$ concentration in the electrolyte, $\text{mol m}^{-3}$
$c_{eq}^s$	equilibrium lithium concentration for species 's', $\text{mol m}^{-3}$
$c_{\max}$	maximum lithium concentration in LFP particles, $\text{mol m}^{-3}$
$C$	current needed to completely discharge the electrode in an hour
$D_i$	diffusion coefficient of $\text{Li}^+$ in phase i, $\text{m}^2 \text{s}^{-1}$
$D_e$	diffusion coefficient of the electrolyte, $\text{m}^2 \text{s}^{-1}$
$f_{\pm}$	mean molar salt activity coefficient
$i_0$	exchange current density, $\text{A m}^{-2}$
$I$	discharge current, A
$i_0$	Exchange current density, $\text{A m}^{-2}$
$i_n$	intercalation current density, $\text{A m}^{-2}$
$k$	kinetic rate constant
$Q$	discharge capacity, A h
$r_i^{\alpha \rightarrow \beta}$	position of the phase boundary when transforming from $\alpha$ to $\beta$ phase, m
$r_i^{\beta \rightarrow \alpha}$	position of the phase boundary when transforming from $\beta$ to $\alpha$ phase, m
$R_g$	gas constant, $8.3145 \text{ J mol}^{-1} \text{ K}^{-1}$
$R$	radius of LFP particles, m
$S$	geometric area of the electrode, $\text{m}^2$
SOC	state of charge
$t$	time, s
$t_+^0$	transference number of the electrolyte
$T$	temperature, K
$U$	equilibrium potential of the electrode, V
bc	Boundary condition
PDE	Partial Differential Equation

#### Greek letters

$\alpha$	Lithium poor phase of $\text{LiFePO}_4$
$\beta$	Lithium rich phase of $\text{LiFePO}_4$
$\alpha_a, \alpha_c$	Transfer coefficient
$\Phi_e, \Phi_s$	liquid or solid phase potential, V
$\delta_p, \delta_s$	electrode or separator thickness, m
$\varepsilon_e$	Volume fraction of electrolyte
$\kappa_e$	Conductivity of the electrolyte, $\text{S m}^{-1}$
$\sigma_s$	Conductivity of the solid phase, $\text{S m}^{-1}$
$\Omega$	Physical domain of $\alpha$ or $\beta$ phase in the particle
$v^{s \rightarrow p}$	Velocity of interface for transforming from source to product

#### Superscript

ref	reference state at 298.15 K
eff	effective property

s	source
p	product

#### Subscript

app	applied
disch	discharge

#### References

- [1] A.K. Padhi, K.S. Nanjundaswamy, J.B. Goodenough, J. Electrochem. Soc. 144 (1997) 1188.
- [2] M. Thackeray, Nat. Mater. 1 (2002) 81.
- [3] M. Takahashi, H. Ohtsuka, K. Akuto, Y. Sakurai, J. Electrochem. Soc. 152 (2005) A899.
- [4] K. Striebel, J. Shim, V. Srinivasan, J. Newman, J. Electrochem. Soc. 152 (2005) A664.
- [5] N. Ravet, A. Abouimrane, M. Armand, Nat. Mater. 2 (2003) 702.
- [6] J.M. Tarascon, M. Armond, Nature 414 (2011) 359.
- [7] N. Ravet, J.B. Goodenough, S. Besner, M. Simoneau, P. Hovington, M. Armand, The Electrochemical Society Meeting Abstracts, Abstract 127, 1999, Honolulu, HI.
- [8] N. Ravet, Y. Chouinard, J.F. Magnan, S. Besner, M. Gauthier, M. Armand, J. Power Sources 97–98 (2001) 503.
- [9] A. Yamada, S.C. Chung, K. Hinokuma, J. Electrochem. Soc. 148 (2001) A224.
- [10] C. Delacourt, P. Poizot, S. Levasseur, C. Masquelier, Electrochem. Solid-state Lett. 9 (2006) A352.
- [11] B. Xing-Long Wu, L.Y. Jiang, F.F. Cao, Y. Guo, L.J. Wan, Adv. Mater. 21 (2009) 2710.
- [12] S.-Y. Chung, J.T. Bloking, Y.-M. Chiang, Nat. Mater. 1 (2002) 123.
- [13] Q. Zhang, R.E. White, J. Electrochem. Soc. 154 (2007) A587.
- [14] V. Srinivasan, J. Newman, J. Electrochem. Soc. 151 (2004) A1517.
- [15] V. Srinivasan, J. Newman, J. Electrochem. Soc. 151 (2004) A1530.
- [16] C. Wang, U.S. Kasavajjula, P.E. Arce, J. Phys. Chem. C 111 (2007) 16656.
- [17] U.S. Kasavajjula, C. Wang, P.E. Arce, J. Electrochem. Soc. 155 (2008) A866.
- [18] S. Dargaville, T.W. Farrell, J. Electrochem. Soc. 157 (2010) A830.
- [19] G.K. Singh, G. Ceder, M.Z. Bazant, Electrochim. Acta 53 (2008) 7599.
- [20] B.C. Han, A. Van der Ven, D. Morgan, G. Ceder, Electrochim. Acta 49 (2004) 4691.
- [21] D. Burch, G. Singh, G. Ceder, M.Z. Bazant, Solid State Lett. 139 (2008) 95.
- [22] D. Burch, M.Z. Bazant, Nano Lett. 9 (2009) 3795.
- [23] D.A. Cogswell, M.Z. Bazant, ACS Nano 6 (2012) 2215.
- [24] K.E. Thomas-Alyea, ECS Trans. 1613 (2008) 155.
- [25] I.V. Thorat, T. Joshi, K. Zaghib, J.N. Harb, D.R. Wheeler, J. Electrochem. Soc. 158 (2011) A1185.
- [26] M. Safari, C. Delacourt, J. Electrochem. Soc. 158 (2011) A63.
- [27] M. Safari, C. Delacourt, J. Electrochem. Soc. 158 (2011) A562.
- [28] M. Kassem, J. Bernard, R. Revel, S. Pélissier, F. Duclaud, C. Delacourt, J. Power Sources 208 (2012) 296.
- [29] V. Srinivasan, J. Newman, Electrochem. Solid-state Lett. 9 (2006) A110.
- [30] J.L. Dodd, Ph.D. Dissertation, California Institute of Technology, 2007.
- [31] C.V. Ramana, A. Mauger, F. Gendron, C.M. Julien, K. Zaghib, J. Power Sources 187 (2009) 555.
- [32] M. Yoshio, H. Tanaka, K. Tominaga, H. Noguchi, J. Power Sources 40 (1992) 347.
- [33] M. Doyle, T.F. Fuller, J. Newman, J. Electrochem. Soc. 140 (1993) 1526.
- [34] T.F. Fuller, M. Doyle, J. Newman, J. Electrochem. Soc. 141 (1994) 1.
- [35] K.E. Thomas, J. Newman, R.M. Darling, in: W. vanSchalkwijk, B. Scrosati (Eds.), Advances in Lithium Ion Batteries, Kluwer Academic Publishers, New York, 2002, pp. 345–392.
- [36] V. Ramadesigan, P.W.C. Northrop, S. De, S. Santhanagopalan, R.D. Braatz, V.R. Subramanian, J. Electrochem. Soc. 159 (2012) R31.
- [37] P.M. Gomadam, J.W. Weidner, R.A. Dougal, R.E. White, J. Power Sources 110 (2002) 267.
- [38] J.B. Collins, Phys. Rev. B 31 (1985) 6119.
- [39] A. Kirsch, Introduction to the Mathematical Theory of Inverse Problems, Applied Mathematical Sciences Series 120, Springer Verlag, Berlin–Heidelberg–New York, 1996.
- [40] T.C. Illingworth, I.O. Golosnoy, J. Comput. Phys. 209 (2005) 207.
- [41] M. Cherkaoui, M. Berveiller, X. Lemoine, Int. J. Plasticity 16 (2000) 1215.
- [42] K. Jagannathan, K. Raghunathan, J. Electrochem. Soc. 159 (2012) A26.
- [43] H.G. Landau, Q.J. Mech. Appl. Math. 8 (1950) 81.
- [44] COMSOL website. <http://www.comsol.com>, April 2013.
- [45] M. Doyle, J. Newman, A.S. Gozdz, C.N. Schmutz, J. Tarascon, J. Electrochem. Soc. 143 (1996) 1890.
- [46] T.R. Ferguson, M.Z. Bazant, J. Electrochem. Soc. 159 (2012) A1967.
- [47] S. Renganathan, G. Sikha, S. Santhanagopalan, R.E. White, J. Electrochem. Soc. 157 (2010) A155.
- [48] D. Wang, X. Wu, Z. Wang, L. Chen, J. Power Sources 140 (2005) 125.
- [49] M.A. Roscher, J. Vetter, D.U. Sauer, J. Power Sources 191 (2009) 582.
- [50] G. Ouvrard, M. Zerrouki, P. Soudan, B. Lestrieza, C. Masquelier, M. Morcrette, S. Hamelet, S. Belin, A.M. Flank, F. Baudele, J. Power Sources 229 (2013) 16.



- [51] M. Dubarry, B.Y. Liaw, J. Power Sources 194 (2009) 541.
- [52] Y. Zhang, C.-Y. Wang, X. Tang, J. Power Sources 196 (2011) 1513.
- [53] J. Wang, P. Liu, J. Hicks-Garner, E. Sherman, S. Soukiazian, M. Verbrugge, H. Tataria, J. Musser, P. Finamore, J. Power Sources 196 (2011) 3942.
- [54] Y. Ye, Y. Shi, A.A.O. Tay, J. Power Sources 217 (2012) 509.
- [55] M.A. Roscher, D.U. Sauer, J. Power Sources 196 (2011) 331.
- [56] W.C. Chueh, F. El Gabaly, J.D. Sugar, N.C. Bartelt, A.H. McDaniel, K.R. Fenton, K.R. Zavadil, T. Tyliczszak, W. Lai, K.F. McCarty, Nano Lett. 13 (2013) 866.